

Magnetic data radial inversion for 3-D source geometry estimation

L.B. Vital^{1*}

¹ *Observatório Nacional, Gal. José Cristino, 77, São Cristóvão, Rio de Janeiro, 20921-400, Brazil*

SUMMARY

We present a method for inverting total-field anomaly data to estimate the geometry of a 3D complex geological source in subsurface. The method assumes total-magnetization direction is known. We use an ensemble of vertically juxtaposed 3D right prisms to approximate the shape of the geological source. Each prism has a known homogeneous magnetization and an unknown regular polygon as its horizontal cross-sections. The vertices of the polygons approximately describe the edges of horizontal depth slices of the source. All prisms' polygons have the same fixed number of vertices, which are equally spaced with central angles from 0° to 360° and horizontally described by polar coordinates associated to an arbitrary origin within each prism. We used a validation test to define the total-magnetization intensity and the depth to the top of the magnetic source. This test uses successive inversions for a range of both parameters, where we set a pair of them for each inverted solution. These parameters are defined based on the minimization of the goal function. The lower the goal function, the better the data fit. The method estimates the radii of all vertices, the horizontal Cartesian coordinates of all arbitrary origins, and the depth extent of the prisms defining the shape of the interpretation model. We impose zeroth- and first-order Tikhonov regularizations as constraints on the shape of the estimated model to stabilize the inverse problem. The method allows estimating both vertical and inclined sources by a suitable use of first-order Tikhonov regularization. This regularization can be applied on either all or few parameters excluding the depth extent of the prisms. The tests on synthetic and field data show the efficiency of the method on retrieving the shape of a complex geologic source.

Key words: Numerical solutions; Inverse theory; Magnetic anomalies.

1 INTRODUCTION

The interpretation of a 3D magnetic survey measured above the surface of the earth is an important challenge in exploration geophysics. Many authors developed different strategies to interpret magnetic data quantitatively. The nonuniqueness of the magnetic inversion is well-known so that several subsurface sources can reproduce the same magnetic dataset with the same accuracy. Necessarily, a priori information is required in the inversion process to overcome this difficulty. By introducing it, the family of mathematically acceptable models should decrease and be more coherent to the local geology.

There are groups of approaches that deal differently with such nonuniqueness of the magnetic inverse problem. The prior information available can determine a suitable approach depending on the desired outcome of inversion. The first group approximates the magnetic source by a geometrically simple causative body with a small number of parameters that define the geometry and the physical property. Commonly, this approach consists of a nonlinear optimization problem with a small family of possible solutions due to the very restrictive parametrization (Ballantyne 1980; Bhattacharyya 1980; Silva & Hohmann 1983).

The second group composes the vast majority of magnetic inversion methods. These methods divide the subsurface in a grid of rectangular prisms that have magnetization direction aligned with the local main field of the earth (Cribb 1976; Li & Oldenburg 1996; Pilkington 1997). In these methods, the magnetic susceptibility is a parameter in the inversion, considered isotropic within each prism. Additionally, some of these methods allow a magnetization direction different from the local main field direction (Pignatelli et al. 2006). In this case, instead of estimating susceptibility, these methods estimate the total-magnetization intensity within each prism. The magnetic sources in the subsurface are imagined by the estimated susceptibility distribution or magnetization intensity supporting the geological interpretation. Theoretically, these methods are capable of recovering the geometry of complex sources. However, they are characterized by a high computational cost due to the solution of large linear systems. Another disadvantage of these methods is the necessity to impose prior information to overcome problems of nonuniqueness and instability due to a large number of parameters in the inversion.

The third group of total-field anomaly inversion estimates the geometries or boundaries of a magnetic source by assuming some knowledge about the physical property. The method proposed by Wang & Hansen (1990) estimates, in the frequency domain, the spacial position of vertices defining a polyhedron body. Among the few studies in this group, Li et al. (2017) have developed a multiple level-set method to estimate the shape of a 3D magnetic source. This method represents the geological structure by a set of causative bodies with uniform magnetic susceptibility. According to the authors, this

method is only applicable to magnetic data produced by sources with weak induced magnetization and known magnetic susceptibility. However, these methods have a small number of parameters for inversion than the second group. In addition, the inherent nonuniqueness of the magnetic inversion for these methods is not severe in comparison to the other groups due to the flexibility of the parametrization. As noticeable, the lack of works on 3D magnetic inversion presents a great challenge in the area of the potential fields.

The main difficulty in magnetic inversion to estimate the shape of a 3D magnetic source is that prior information about the physical property and position of the body is necessary as input. If available, prior information can help the algorithm to deal with fewer parameters in the inversion process. In other words, the whole process would be faster and more suitable for the geological configuration. Moreover, the choice of the best solution would be easier due to the smaller subset of possible solutions. Consequently, the inverted boundaries of the body can delineate more realistically the magnetic source. We thus are challenged to develop an algorithm that requires the total-magnetization direction only and retrieves complex geometries for an isolated source.

We present an algorithm to estimate the geometry of an isolated magnetic 3D source by inverting total-field anomaly data with known total-magnetization direction. The prisms have the same depth extent and total-magnetization intensity that are a parameter and a constant in the inversion process, respectively. The method estimates the radii connecting an arbitrary origin and the vertices of the regular polygon that describes the horizontal cross-section of the prisms. Also, the algorithm estimates the Cartesian coordinates of the arbitrary origin of the prisms polygons. The magnetic source is approximated by a set of vertically juxtaposed polygonal prisms to estimate the shape of the source. The method is an extension for magnetic data of those presented by Oliveira Jr. et al. (2011) and Oliveira Jr. et al. (2015) for inversion of gravity and gravity-gradient data, respectively. However, differently from those authors, we estimate the thickness of all prisms defining the interpretation model. Additionally, we introduced a validation test using successive inversions for ranges of depth to the top and the total-magnetization intensity of the source and choosing them based on the lower values of the objective function. To obtain a stable solutions, we introduced a set of six smoothness constraints following the strategy of Oliveira Jr. et al. (2011) and a new minimum Euclidean constraint on the depth extent of the prisms. Ultimately, tests on synthetic total-field anomaly data and a field application on the Anitápolis alkaline complex, Santa Catarina, Brazil, support the efficiency of our method.

2 METHODOLOGY

2.1 Forward problem

Let \mathbf{d}^o be the observed data vector, whose i th element d_i^o , $i = 1, \dots, N$, is the total-field anomaly produced by a 3-D source (Fig. 1a) at the point (x_i, y_i, z_i) of a Cartesian coordinate system with x , y and z axes pointing to north, east and down, respectively. We assume that the direction of the total magnetization vector of the source is constant and known. We approximate the volume of the source by a set of L vertically juxtaposed 3-D prisms (Fig. 1b) by following the same approach of Oliveira Jr. et al. (2011) and Oliveira Jr. & Barbosa (2013). The depth to the top of the shallowest prism is defined by z_0 and m_0 is the constant total-magnetization intensity of all prisms. The horizontal cross-section of each prism is described by a polygon with a fixed number V of vertices equally spaced from 0° to 360° , which are described in polar coordinates referred to an internal origin O^k . The radii of the vertices $(r_j^k, j = 1, \dots, V, k = 1, \dots, L)$, the horizontal coordinates $(x_0^k$ and $y_0^k, k = 1, \dots, L)$ of the origins $O^k, k = 1, \dots, L$, and the depth extent dz of the L vertically stacked prisms (Fig. 1b) are arranged in a $M \times 1$ parameter vector \mathbf{p} , $M = L(V + 2) + 1$, given by

$$\mathbf{p} = \begin{bmatrix} \mathbf{r}^{1\top} & x_0^1 & y_0^1 & \dots & \mathbf{r}^{L\top} & x_0^L & y_0^L & dz \end{bmatrix}^\top, \quad (1)$$

where “ \top ” denotes transposition and \mathbf{r}^k is a $V \times 1$ vector containing the radii r_j^k of the k th prism. Let $\mathbf{d}(\mathbf{p})$ be the predicted data vector, whose i th element

$$d_i(\mathbf{p}) \equiv \sum_{k=1}^L f_i^k(\mathbf{r}^k, x_0^k, y_0^k, dz, z_1^k, m_0), \quad i = 1, \dots, N, \quad (2)$$

is the total-field anomaly produced by the ensemble of L prisms at the i th observation point (x_i, y_i, z_i) . In eq. 2, $f_i^k(\mathbf{r}^k, x_0^k, y_0^k, dz, z_1^k, m_0)$ is the total-field anomaly produced, at the observation point (x_i, y_i, z_i) , by the k th prism, with depth to the top $z_1^k = z_0 + (k - 1)dz$. We calculate $d_i(\mathbf{p})$ (eq. 2) by using the Python package Fatiando a Terra (Uieda et al. 2013), which implements the formulas proposed by Plouff (1976).

2.2 Inverse problem formulation

The total-magnetization of the source m_0 and depth to the top of the shallowest prism z_0 are hyperparameters of the inversion, i. e., they are not estimated during the inversion, but their value influences the final solution. Given a set of tentative values for m_0 and z_0 , we solve a constrained non-linear problem to estimate the parameter vector \mathbf{p} (eq. 1) by minimizing the goal function

$$\Gamma(\mathbf{p}) = \phi(\mathbf{p}) + \sum_{\ell=1}^7 \alpha_\ell \varphi_\ell(\mathbf{p}), \quad (3)$$

subject to

$$p_l^{min} < p_l < p_l^{max}, \quad l = 1, \dots, M, \quad (4)$$

where $\varphi(\mathbf{p})$ is the data-misfit function given by

$$\phi(\mathbf{p}) = \frac{1}{N} \|\mathbf{d}^o - \mathbf{d}(\mathbf{p})\|_2^2, \quad (5)$$

which represents the normalized squared Euclidean norm of the difference between the observed data vector \mathbf{d}^o and the predicted data vector $\mathbf{d}(\mathbf{p})$, α_ℓ is a positive number representing the weight of the ℓ th constraint function $\varphi_\ell(\mathbf{p})$ and p_l^{min} and p_l^{max} are, respectively, the lower and upper limits for the l th element p_l of the parameter vector \mathbf{p} (eq. 1). These limits are defined by the interpreter based on both the horizontal extent of the magnetic anomaly and the knowledge about the source.

To solve our nonlinear inverse problem, we use a gradient-based method and, consequently, we need to define the gradient vector $\nabla\Gamma(\mathbf{p})$ and Hessian matrix $\mathbf{H}(\mathbf{p})$ of the goal function $\Gamma(\mathbf{p})$ (eq. 3):

$$\nabla\Gamma(\mathbf{p}) = \nabla\phi(\mathbf{p}) + \sum_{\ell=1}^7 \alpha_\ell \nabla\varphi_\ell(\mathbf{p}) \quad (6)$$

and

$$\mathbf{H}(\mathbf{p}) = \mathbf{H}_\phi(\mathbf{p}) + \sum_{\ell=1}^7 \alpha_\ell \mathbf{H}_\ell, \quad (7)$$

where

$$\nabla\phi(\mathbf{p}) = -\frac{2}{N} \mathbf{G}(\mathbf{p})^\top [\mathbf{d}^o - \mathbf{d}(\mathbf{p})] \quad (8)$$

and

$$\mathbf{H}_\phi(\mathbf{p}) = \frac{2}{N} \mathbf{G}(\mathbf{p})^\top \mathbf{G}(\mathbf{p}) \quad (9)$$

are the gradient vector of the Hessian matrix of the misfit function $\phi(\mathbf{p})$ (eq. 5), respectively, the terms $\nabla\varphi_\ell(\mathbf{p})$ and \mathbf{H}_ℓ , $\ell = 1, \dots, 7$, are the gradient vectors and Hessian matrices of the constraint functions, respectively, and $\mathbf{G}(\mathbf{p})$ is an $N \times M$ matrix whose element ij is the derivative of the predicted data $d_i(\mathbf{p})$ (eq. 2) with respect to the j element p_j of the parameter vector \mathbf{p} (eq. 1). Details about the constraint functions $\varphi_\ell(\mathbf{p})$, $\ell = 1, \dots, 7$, as well as the numerical procedure to solve this nonlinear inverse problem are given in the following sections.

2.3 Constraint functions

We have divided the constraint functions $\varphi_\ell(\mathbf{p})$ (eq. 3), $\ell = 1, \dots, 7$, used here to obtain stable solutions and introduce a priori information about the magnetic source into three groups.

2.3.1 Smoothness constraints

This group is formed by variations of the first-order Tikhonov regularization (Aster et al. 2019, p. 103) and impose smoothness on the radii r_j^k and the Cartesian coordinates x_0^k and y_0^k of the origin O^k , $j = 1, \dots, V$, $k = 1, \dots, L$, defining the horizontal section of each prism (Fig.1b). They were proposed by Oliveira Jr. et al. (2011) and Oliveira Jr. & Barbosa (2013) and play a very role in introducing a prior information about the shape of the source.

The first constraint of this group is the *Smoothness constraint on the adjacent radii defining the horizontal section of each vertical prism*. This constraint imposes that adjacent radii r_j^k and r_{j+1}^k within each prism must be close to each other. It forces the estimated prism to be approximately cylindrical. Mathematically, the constraint is given by

$$\begin{aligned}\varphi_1(\mathbf{p}) &= \sum_{k=1}^L \left[(r_V^k - r_1^k)^2 + \sum_{j=1}^{V-1} (r_j^k - r_{j+1}^k)^2 \right] \\ &= \mathbf{p}^\top \mathbf{R}_1^\top \mathbf{R}_1 \mathbf{p} ,\end{aligned}\quad (10)$$

where

$$\mathbf{S}_1 = \mathbf{I}_L \otimes \begin{bmatrix} (\mathbf{I}_V - \mathbf{D}_V^\top) & \mathbf{0}_{V \times 2} \end{bmatrix} , \quad (11)$$

$\mathbf{0}_{LV \times 1}$ is an $LV \times 1$ vector with null elements, \mathbf{I}_L is the identity matrix of order L , “ \otimes ” denotes the Kronecker product (Horn & Johnson 1991, p. 243), $\mathbf{0}_{V \times 2}$ is a $V \times 2$ matrix with null elements, \mathbf{I}_V is the identity matrix of order V and \mathbf{D}_V^\top is the upshift permutation matrix of order V (Golub & Loan 2013, p. 20). The gradient and Hessian of function $\varphi_1(\mathbf{p})$ (eq. 10) are given by:

$$\nabla \varphi_1(\mathbf{p}) = 2\mathbf{R}_1^\top \mathbf{R}_1 \mathbf{p} , \quad (12)$$

and

$$\mathbf{H}_1(\mathbf{p}) = 2\mathbf{R}_1^\top \mathbf{R}_1 . \quad (13)$$

The second constraint of this group is the *Smoothness constraint on the adjacent radii of the vertically adjacent prisms*, which imposes that adjacent radii r_j^k and r_j^{k+1} within vertically adjacent prisms must be close to each other. This constraint forces the shape of all prisms to be similar to each other and is given by

$$\begin{aligned}\varphi_2(\mathbf{p}) &= \sum_{k=1}^{L-1} \left[\sum_{j=1}^V (r_j^{k+1} - r_j^k)^2 \right] \\ &= \mathbf{p}^\top \mathbf{R}_2^\top \mathbf{R}_2 \mathbf{p}\end{aligned}\quad (14)$$

where

$$\mathbf{R}_2 = \begin{bmatrix} \mathbf{S}_2 & \mathbf{0}_{(L-1)V \times 1} \end{bmatrix}_{(L-1)V \times M}, \quad (15)$$

$$\mathbf{S}_2 = \left(\begin{bmatrix} \mathbf{I}_{L-1} & \mathbf{0}_{(L-1) \times 1} \end{bmatrix} - \begin{bmatrix} \mathbf{0}_{(L-1) \times 1} & \mathbf{I}_{L-1} \end{bmatrix} \right) \otimes \begin{bmatrix} \mathbf{I}_V & \mathbf{0}_{V \times 2} \end{bmatrix}, \quad (16)$$

$\mathbf{0}_{(L-1)V \times 1}$ is an $(L-1)V \times 1$ vector with null elements, $\mathbf{0}_{(L-1) \times 1}$ is an $(L-1) \times 1$ vector with null elements and \mathbf{I}_{L-1} is the identity matrix of order $L-1$. The gradient and Hessian of function $\varphi_2(\mathbf{p})$ (eq. 14) are given by:

$$\nabla \varphi_2(\mathbf{p}) = 2\mathbf{R}_2^\top \mathbf{R}_2 \mathbf{p}, \quad (17)$$

and

$$\mathbf{H}_2(\mathbf{p}) = 2\mathbf{R}_2^\top \mathbf{R}_2. \quad (18)$$

The last constraint of this group is the *Smoothness constraint on the horizontal position of the arbitrary origins of the vertically adjacent prisms*. This constraint imposes that the estimated horizontal Cartesian coordinates (x_0^k, y_0^k) and (x_0^{k+1}, y_0^{k+1}) of the origins O^k and O^{k+1} of adjacent prisms must be close to each other. It forces the prisms to be vertically aligned. This constraint is given by

$$\begin{aligned} \varphi_3(\mathbf{p}) &= \sum_{k=1}^{L-1} \left[(x_0^{k+1} - x_0^k)^2 + (y_0^{k+1} - y_0^k)^2 \right], \\ &= \mathbf{p}^\top \mathbf{R}_3^\top \mathbf{R}_3 \mathbf{p} \end{aligned}, \quad (19)$$

where

$$\mathbf{R}_3 = \begin{bmatrix} \mathbf{S}_3 & \mathbf{0}_{(L-1)2 \times 1} \end{bmatrix}_{(L-1)2 \times M}, \quad (20)$$

$$\mathbf{S}_3 = \left(\begin{bmatrix} \mathbf{I}_{L-1} & \mathbf{0}_{(L-1) \times 1} \end{bmatrix} - \begin{bmatrix} \mathbf{0}_{(L-1) \times 1} & \mathbf{I}_{L-1} \end{bmatrix} \right) \otimes \begin{bmatrix} \mathbf{0}_{2 \times V} & \mathbf{I}_2 \end{bmatrix}, \quad (21)$$

$\mathbf{0}_{(L-1)2 \times 1}$ is an $(L-1)2 \times 1$ vector with null elements, $\mathbf{0}_{2 \times V}$ is a $2 \times V$ matrix with null elements and \mathbf{I}_2 is the identity matrix of order 2. The gradient and Hessian of function $\varphi_3(\mathbf{p})$ (eq. 19) are given by:

$$\nabla \varphi_3(\mathbf{p}) = 2\mathbf{R}_3^\top \mathbf{R}_3 \mathbf{p}, \quad (22)$$

and

$$\mathbf{H}_3(\mathbf{p}) = 2\mathbf{R}_3^\top \mathbf{R}_3. \quad (23)$$

2.3.2 Equality constraints

This group is formed by two constraints that were proposed by Oliveira Jr. et al. (2011) and Oliveira Jr. & Barbosa (2013) by following the same approach proposed Barbosa et al. (1997) and ?. They introduce a priori information about the shallowest prism and are suitable for outcropping sources.

The *Source's outcrop constraint* imposes that the horizontal cross-section of the shallowest prism must be close to the intersection of the geologic source with the known outcropping boundary. The matrix form of the this constraint is given by

$$\begin{aligned}\varphi_4(\mathbf{p}) &= \left[(x_0^1 - x_0^0)^2 + (y_0^1 - y_0^0)^2 + \sum_{j=1}^V (r_j^1 - r_j^0)^2 \right] , \\ &= (\mathbf{R}_4\mathbf{p} - \mathbf{a})^\top (\mathbf{R}_4\mathbf{p} - \mathbf{a})\end{aligned}\quad (24)$$

where \mathbf{a} is a vector containing the radii and the horizontal Cartesian coordinates of the polygon defining the outcropping boundary

$$\mathbf{a} = \begin{bmatrix} \tilde{r}_1^0 & \dots & \tilde{r}_V^0 & \tilde{x}_0^0 & \tilde{y}_0^0 \end{bmatrix}^\top , \quad (25)$$

and

$$\mathbf{R}_4 = \begin{bmatrix} \mathbf{I}_{V+2} & \mathbf{0}_{(V+2) \times (M-V-2)} \end{bmatrix}_{(V+2) \times M} , \quad (26)$$

where \mathbf{I}_{V+2} is the identity matrix of order $V+2$ and $\mathbf{0}_{(V+2) \times (M-V-2)}$ is a matrix with null elements. The gradient and Hessian of function $\varphi_4(\mathbf{p})$ (eq. 24) are given by:

$$\nabla \varphi_4(\mathbf{p}) = 2\mathbf{R}_4^\top (\mathbf{R}_4\mathbf{p} - \mathbf{a}) , \quad (27)$$

and

$$\mathbf{H}_4(\mathbf{p}) = 2\mathbf{R}_4^\top \mathbf{R}_4 . \quad (28)$$

The *Source's horizontal location constraint* imposes that the horizontal Cartesian coordinates of the origin within the shallowest prism must be as close as possible to a known outcropping point. The matrix form of the this constraint is given by

$$\begin{aligned}\varphi_5(\mathbf{p}) &= \left[(x_0^1 - x_0^0)^2 + (y_0^1 - y_0^0)^2 \right] , \\ &= (\mathbf{R}_5\mathbf{p} - \mathbf{b})^\top (\mathbf{R}_5\mathbf{p} - \mathbf{b})\end{aligned}\quad (29)$$

where \mathbf{b} is a vector containing the horizontal Cartesian coordinates of the outcropping point

$$\mathbf{b} = \begin{bmatrix} \tilde{x}_0^0 & \tilde{y}_0^0 \end{bmatrix}^\top , \quad (30)$$

and

$$\mathbf{R}_5 = \begin{bmatrix} \mathbf{0}_{2 \times V} & \mathbf{I}_2 & \mathbf{0}_{2 \times (M-V-2)} \end{bmatrix}_{2 \times M} , \quad (31)$$

where \mathbf{I}_2 is the identity matrix of order 2 and $\mathbf{0}_{2 \times (M-V-2)}$ and $\mathbf{0}_{2 \times V}$ are matrices with null elements. The gradient and Hessian of function $\varphi_5(\mathbf{p})$ (eq. 29) are given by:

$$\nabla \varphi_5(\mathbf{p}) = 2\mathbf{R}_5^\top (\mathbf{R}_5\mathbf{p} - \mathbf{b}) , \quad (32)$$

and

$$\mathbf{H}_5(\mathbf{p}) = 2\mathbf{R}_5^T \mathbf{R}_5 . \quad (33)$$

2.3.3 Minimum Euclidean norm constraints

Two constraints use the zeroth-order Tikhonov regularization with the purpose of obtaining stable solutions without necessarily introducing significant a priori information about the source.

The *Minimum Euclidean norm of the radii* imposes that all estimated radii within each prism must be close to null values. This constraint were proposed by Oliveira Jr. et al. (2011) and Oliveira Jr. & Barbosa (2013) and can be rewritten in matrix form as follows

$$\begin{aligned} \varphi_6(\mathbf{p}) &= \sum_{k=1}^L \sum_{j=1}^V \left(r_j^k \right)^2 , \\ &= \mathbf{p}^T \mathbf{R}_6^T \mathbf{R}_6 \mathbf{p} \end{aligned} \quad (34)$$

where

$$\mathbf{R}_6 = \begin{bmatrix} \mathbf{S}_6 & \mathbf{0}_{(M-1) \times 1} \\ \mathbf{0}_{1 \times (M-1)} & 0 \end{bmatrix}_{M \times M} , \quad (35)$$

and

$$\mathbf{S}_6 = \begin{bmatrix} \mathbf{I}_V & \mathbf{0}_{V \times 2} \\ \mathbf{0}_{2 \times V} & \mathbf{I}_2 \end{bmatrix}_{(V+2) \times (V+2)} . \quad (36)$$

The gradient and Hessian of function $\varphi_6(\mathbf{p})$ (eq. 34) are given by:

$$\nabla \varphi_6(\mathbf{p}) = 2\mathbf{R}_6^T \mathbf{R}_6 \mathbf{p} , \quad (37)$$

and

$$\mathbf{H}_6(\mathbf{p}) = 2\mathbf{R}_6^T \mathbf{R}_6 . \quad (38)$$

The other constraint, the *Minimum Euclidean norm of the depth extent*, imposes that the depth extent of all prisms must be close to zero. We present this constraint to introduce a priori information about the maximum depth of the source. It is given by

$$\begin{aligned} \varphi_7(\mathbf{p}) &= dz^2 \\ &= \mathbf{p}^T \mathbf{R}_7^T \mathbf{R}_7 \mathbf{p} \end{aligned} , \quad (39)$$

where

$$\mathbf{R}_7 = \begin{bmatrix} \mathbf{0}_{(M-1) \times (M-1)} & \mathbf{0}_{(M-1) \times 1} \\ \mathbf{0}_{1 \times (M-1)} & 1 \end{bmatrix}_{M \times M} . \quad (40)$$

The gradient and Hessian of function $\varphi_7(\mathbf{p})$ (eq. 39) are given by:

$$\nabla \varphi_7(\mathbf{p}) = 2\mathbf{R}_7^\top \mathbf{R}_7 \mathbf{p} , \quad (41)$$

and

$$\mathbf{H}_7(\mathbf{p}) = 2\mathbf{R}_7^\top \mathbf{R}_7 . \quad (42)$$

2.4 Computational procedures

To estimate the parameter vector \mathbf{p} (eq. 1) that minimizes the goal function $\Gamma(\mathbf{p})$ (eq. 3), subjected to the inequality constraint (eq. 4), we use the Levenberg-Marquardt method (e.g., Aster et al. 2019, p. 240). This is an iterative gradient-based method that, at each iteration k , updates the estimated parameter vector $\hat{\mathbf{p}}_{(k)}$ (where the superscript hat “ $\hat{\cdot}$ ” denotes estimated) to obtain new a estimated parameter vector $\hat{\mathbf{p}}_{(k+1)}$. We compute this update by following the same strategy of Barbosa et al. (1999b), Oliveira Jr. et al. (2011) and Oliveira Jr. & Barbosa (2013) to incorporate the inequality constraint (eq. 4). This strategy consists in transforming each element p_l of the estimated parameter vector $\hat{\mathbf{p}}_{(k)}$ into the element p_l^\dagger of a new vector $\hat{\mathbf{p}}_{(k)}^\dagger$ as follows:

$$p_l^\dagger = -\ln \left(\frac{p_l^{max} - p_l}{p_l - p_l^{min}} \right) , \quad (43)$$

where p_l^{min} and p_l^{max} are defined in the inequality constraint (eq. 4). Then, we compute a correction $\Delta\hat{\mathbf{p}}_{(k)}^\dagger$ and a new vector $\hat{\mathbf{p}}_{(k+1)}^\dagger = \hat{\mathbf{p}}_{(k)}^\dagger + \Delta\hat{\mathbf{p}}_{(k)}^\dagger$. Finally, we transform each element p_l^\dagger of $\hat{\mathbf{p}}_{(k+1)}^\dagger$ into the element p_l of the new estimated parameter vector $\hat{\mathbf{p}}_{(k+1)}$ as follows:

$$p_l = p_l^{min} + \left(\frac{p_l^{max} - p_l^{min}}{1 + e^{-p_l^\dagger}} \right) . \quad (44)$$

What follows presents details about how we compute the correction $\Delta\hat{\mathbf{p}}_{(k)}^\dagger$ and a fully description of our algorithm.

2.4.1 Considerations about the weights $\alpha_1 - \alpha_7$

Attributing values to the weights α_ℓ (eq. 3) is an important feature of our method. However, there is no analytical rule to define them and their values can be dependent on the particular characteristics of the interpretation model. To overcome this problem, we normalize the α_ℓ values as follows:

$$\alpha_\ell = \tilde{\alpha}_\ell \frac{E_\phi}{E_\ell}, \quad \ell = 1, \dots, 7, \quad (45)$$

where $\tilde{\alpha}_\ell$ is a positive scalar and E_ϕ/E_ℓ is a normalizing factor. In this equation, E_ℓ represents the trace of the Hessian matrix \mathbf{H}_ℓ (eqs 13, 18, 23, 28, 33, 38, and 42) of the ℓ th constraining function $\varphi_\ell(\mathbf{p})$ (eqs 10, 14, 19, 24, 29, 34, and 39). The constant E_ϕ is the trace of the Hessian matrix $\mathbf{H}_\phi(\mathbf{p}_0)$ (eq.

9) of the misfit function $\phi(\mathbf{p})$ (eq. 5) computed with the initial approximation $\hat{\mathbf{p}}_{(0)}$ for the parameter vector \mathbf{p} (eq. 1) at the beginning of the inversion algorithm. According to this empirical strategy, the weights α_ℓ are defined using the positive scalars $\tilde{\alpha}_\ell$ (eq. 45), which are less dependent on the particular characteristics of the interpretation model.

2.4.2 Inversion algorithm

At each iteration k of our algorithm, the correction $\Delta\hat{\mathbf{p}}_{(k)}^\dagger$ is computed by solving the following linear system:

$$\mathbf{D}_{(k)} \left[\mathbf{D}_{(k)} \mathbf{H}^\dagger(\hat{\mathbf{p}}_{(k)}) \mathbf{D}_{(k)} + \lambda_{(k)} \mathbf{I} \right] \mathbf{D}_{(k)} \Delta\hat{\mathbf{p}}_{(k)}^\dagger = -\nabla\Gamma(\hat{\mathbf{p}}_{(k)}), \quad (46)$$

where $\lambda_{(k)}$ is the a positive scalar adjusted at each iteration (e.g., Aster et al. 2019, p. 240), \mathbf{I} is the identity matrix with order M , $\nabla\Gamma(\hat{\mathbf{p}})$ is the gradient of the goal function (eq. 6) and $\mathbf{H}^\dagger(\hat{\mathbf{p}}_{(k)})$ is a matrix given by

$$\mathbf{H}^\dagger(\hat{\mathbf{p}}_{(k)}) = \mathbf{H}(\hat{\mathbf{p}}_{(k)}) \mathbf{T}(\hat{\mathbf{p}}_{(k)}), \quad (47)$$

where $\mathbf{H}(\hat{\mathbf{p}}_{(k)})$ is the Hessian matrix of the goal function (eq. 7) and $\mathbf{T}(\hat{\mathbf{p}}_{(k)})$ is a diagonal matrix whose element ll is given by

$$t(p_l) = \frac{(p_l^{max} - p_l)(p_l - p_l^{min})}{p_l^{max} - p_l^{min}}, \quad l = 1, \dots, M, \quad (48)$$

with p_l being the l th element of the estimated parameter vector $\hat{\mathbf{p}}_{(k)}$. In eq. 46, $\mathbf{D}_{(k)}$ is a diagonal matrix proposed by Marquardt (1963) for scaling the parameter $\lambda_{(k)}$ at each iteration and improving the convergence of the algorithm. The element ll of this diagonal matrix is given by

$$d_{ll} = \frac{1}{\sqrt{h_{ll}^\dagger}}, \quad (49)$$

where h_{ll}^\dagger is the element ll of the matrix $\mathbf{H}^\dagger(\hat{\mathbf{p}}_{(k)})$ (eq. 47). Figure 3 shows a flowchart of our algorithm.

PAREI AQUI

2.4.3 Practical considerations

Our algorithm depends on several parameters that significantly impact the estimated models and cannot be automatically set without the interpreter's judgment. They are the parameters $\tilde{\alpha}_1, \tilde{\alpha}_2, \tilde{\alpha}_3, \tilde{\alpha}_4, \tilde{\alpha}_5, \tilde{\alpha}_6$, and $\tilde{\alpha}_7$. Based on our practical experience, we suggest some empirical procedures for setting these parameters.

The parameters $\tilde{\alpha}_1$ and $\tilde{\alpha}_2$ impose priori information on the shape of the horizontal cross-section of the prisms. Generally, they have values close to each other varying from 10^{-5} to 10^{-4} . If $\tilde{\alpha}_1 > \tilde{\alpha}_2$ the prisms will have a very smooth horizontal cross-section, close to a circular shape. On the other

hand, if $\tilde{\alpha}_1 < \tilde{\alpha}_2$, than the difference on the shape of the horizontal cross-sections of the estimated model between vertically adjacent prisms will be smooth.

To control the alignment of the estimated model, the parameter $\tilde{\alpha}_3$ should be in a range from 10^{-5} to 10^{-3} . This parameter allows or forbids the estimated model to dip. Empirically, the value for this parameter follows the value for $\tilde{\alpha}_1$ and $\tilde{\alpha}_2$, they are usually close.

The parameter $\tilde{\alpha}_6$ imposes mathematical priori information on the inverse problem to control the convergence of the algorithm. We suggest that the value for this parameter should be two or three orders of magnitude greater than $\tilde{\alpha}_1$ and $\tilde{\alpha}_2$.

To control the depth extent of the estimated model, the parameter $\tilde{\alpha}_7$ should be in a range from 10^{-6} to 10^{-4} . This parameter depends on the depth extent of the initial approximate, it can decrease the depth extent or keep it close to the initial one. Normally, we suggest $\tilde{\alpha}_7 = 10^{-5}$ for a initial value.

An important aspect of our method is the choice of the initial approximation. For simplicity, we use a cylinder shape as an initial approximation located the initial cylinder on the center of the anomaly. We suggest that the cylinder radius should involves a great part, both positive and negative, of the horizontal size of the anomaly. Also, the depth extent dz of the cylinder should be greater than the true source. We suggest that the data produced by the initial approximation fit qualitatively the observations.

3 APPLICATION TO SYNTHETIC DATA

3.1 Simple model test

We have simulated a funnel-shaped source with simple geometry (blue prisms in Figs 4b and 6), which extends from $z_0 = 0$ m to 1600 m along depth and satisfies most of the constraints described in subsection 2.3. It is formed by $L = 8$ prisms, all of them with the same number of vertices $V = 20$, depth extent $dz = 200$ m and horizontal coordinates $(x_0^k, y_0^k) = (0, 0)$ m of the origins O^k , $k = 1, \dots, L$. The radii of all vertices are equal to each other within the same prism and decrease linearly with depth, varying from $r_j^0 = 1920$ m, at the shallowest prism, $r_j^L = 800$ m, at the deepest prism, $j = 1, \dots, V$. All prisms have the same total-magnetization direction with inclination -21.5° , declination -18.7° and intensity $m_0 = 9$ A/m. We calculated the total-field anomaly produced by this simple model on an 100 km^2 area, simulating an airborne survey composed of 21 flight lines that are equally spaced 500 m apart along the y axis, at a constant vertical coordinate $z = -150$ m. At each line, there are 100 observation points spaced 101 m apart along x axis. The total-field anomaly is corrupted with a pseudorandom Gaussian noise having mean $\mu_0 = 0$ nT and standard deviation $\sigma_0 = 5$ nT (Fig. 4a).

We have inverted the synthetic total-field anomaly (Fig. 4a) produced by the simple model and obtained 36 different models. Each model was obtained by using a different pair of depth to the top z_0 and total-magnetization intensity m_0 (Fig. 5). All models were generated by using the true values of total-magnetization inclination and declination, the same interpretation model formed by $L = 5$ prisms, each one with $V = 20$ vertices, and the same weights for the constraining functions: $\tilde{\alpha}_1 = 10^{-4}$, $\tilde{\alpha}_2 = 10^{-4}$, $\tilde{\alpha}_3 = 10^{-4}$, $\tilde{\alpha}_4 = 0$, $\tilde{\alpha}_5 = 0$, $\tilde{\alpha}_6 = 10^{-6}$, and $\tilde{\alpha}_7 = 10^{-4}$. The initial approximation for all models have the same constant radii $r_j^k = 2000$ m, $k = 1, \dots, L$, $j = 1, \dots, V$, the same depth extent $dz = 350$ m and the same origin $(x_0^k, y_0^k) = (0, 0)$ m for all prisms.

Fig. 5 shows that the estimated model obtained by using the true values for depth to the top z_0 and total-magnetization intensity m_0 (represented by the red triangle in Fig. 5) produces the lowest value of goal function $\Gamma(p)$ (eq. 3). Fig. 6a shows that this estimated model (red prisms in Figs 6c and d) not only fits the noise-corrupted data, but also retrieves the geometry of the true model (blue prisms). The inset in Fig. 6a shows that the residuals follow a normal distribution with mean μ and standard deviation σ compatible to μ_0 and σ_0 . The estimated depth extent of each prism is $dz = 297.65$ m, which results in a total depth extent (1485 m) very close to the true one (1600 m). These results illustrate the good performance of our method in an ideal case.

3.2 Complex model test

We have simulated a complex inclined body (blue prisms in Figs 7 and 9), which extends from $z_0 = -300$ m to 5700 m along depth and violates most of the constraints described in subsection 2.3. It is formed by $L = 10$ prisms, all of them with the same number of vertices $V = 30$ and depth extent $dz = 600$ m. The horizontal coordinates of the origins O^k vary linearly from $(x_0^0, y_0^0) = (-250, 750)$ m, at the shallowest prism, to $(x_L^0, y_L^0) = (250, -750)$ m resulting a dip in the direction NW-SE, at the deepest prism. The radii $r_j^k, k = 1, \dots, L, j = 1, \dots, V$, defining the vertices vary from 240 m to 1540 m and also differ from each other within the same prism. All prisms have a constant total magnetization with inclination -50° , declination 9° and intensity $m_0 = 12$ A/m. This total magnetization is based on Zhang et al. (2018) which have estimated the total-magnetization vector for magnetic sources on the Goiás alkaline province (GAP). So, we are simulating an alkaline vertical dipping intrusion. We have calculated the total-field anomaly produced by this complex model on an 100 km^2 area, simulating an airborne survey composed of 18 north-south flight lines distributed from -5000 m to 5000 m along the y axis and a east-west tie line approximately located at $x = 0$ m. The data points are located on the undulated surface shown in Fig. 7a. Notice that both flight and tie lines are not perfectly straight. We added a pseudorandom Gaussian noise having mean μ_0 nT and standard deviation σ_0 nT to the produced total-field anomaly (Fig. 4a).

Actually, they simulate the real survey presented in the following section. To compute the synthetic total-field anomaly, we consider a constant main field with inclination -21.5° and declination -18.7° , which is significantly different from the total-magnetization direction of the complex model. Finally, we have contaminated the synthetic total-field anomaly with a pseudo-random Gaussian noise having mean and standard deviation equal to 0 nT and 5 nT, respectively (Fig. 7a). We have inverted the synthetic total-field anomaly (Fig. 7a) produced by the complex model and to obtain 36 different models. Each model was obtained by using a specific pair of depth to the top z_0 and total-magnetization intensity m_0 (Fig. 8). Differently from the previous simulation with a simple model, the present grid of m_0 and z_0 does not contain the true values (represented by the red triangle in Fig. 8). All models were generated by using the true values of total-magnetization inclination and declination, the same interpretation model formed by $L = 8$ prisms, each one with $V = 15$ vertices, and the same weights for the constraining functions: $\tilde{\alpha}_1 = 10^{-5}$, $\tilde{\alpha}_2 = 10^{-4}$, $\tilde{\alpha}_5 = 10^{-4}$, $\tilde{\alpha}_6 = 10^{-7}$, and $\tilde{\alpha}_7 = 10^{-5}$. The initial approximation for all models have the same constant radii $r_j^k = 800$ m, $k = 1, \dots, L$, $j = 1, \dots, V$, the same depth extent $dz = 650$ m and the same origin $(x_0^k, y_0^k) = (-300, 300)$ m for all prisms.

The pseudo-color map in Fig. 8 shows that the estimated models closer to the true values of m_0 and z_0 are candidate solutions to match the true source. The estimated model obtained by using an

total-magnetization intensity $m_0 = 11.4 \text{ A/m}$ and a depth to the top $z_0 = -320 \text{ m}$ (represented by the cyan diamond in Fig. 8), close to the true values (represented by the red triangle in Fig. 8), produces the lowest value of goal function $\Gamma(\mathbf{p})$ (eq. 3). Fig. 9 shows that this estimated model (red prisms in Figs 9c and d) fits the noise-corrupted data and also retrieves the geometry of the true source (blue prisms), note that the red prisms edges accurately matches the blue prisms ones. The inset in Fig. 6a shows that the residuals follow a normal distribution with mean μ and standard deviation σ compatible to μ_0 and σ_0 . The estimated total depth extent (5597.7 m) and volume (11.0 km³) are underestimated but it is still close to the true values (6000 m and 12.60 km³). These results show that our method can also be very useful to interpret complex sources, even if they do not perfectly satisfy the constraints imposed to solve the nonlinear inverse problem.

4 APPLICATION TO FIELD DATA

We applied our method to interpret the total-field anomaly data provided by CPRM and acquired by Lasa Prospecções S.A. over the Anitápolis complex in the state of Santa Catarina, Brazil (colocar mapa). The total-field anomaly data were corrected from daytime variation and subtracted from the main field of the Earth using the IGRF. Anitápolis is an intrusive complex in southern Brazil formed by alkaline-carbonatitic rocks (Gomes et al. 2018). The flight was at an elevation of 100 m above the terrain, the N–S and E–W lines were spaced 500 m and 10,000 m, respectively. Fig 10b shows GPS height of the acquisition and the horizontal coordinates referred to the WGS84 datum. We processed the data by applying a regional separation using a second-order polynomial fit. To attenuate the non-dipolar effects present in the data, we applied the equivalent layer (Dampney 1969; Emilia 1973) to continue the anomaly upward to a constant height $z = -2000$ m (Fig. 10a). The upward continued data were calculated in a regular grid of 50×50 points equally spaced from 6916 km to 6926 km in x axis and 683 km to 693. in y axis. The main field direction in the area at that time has an inclination and declination ($-37.05^\circ, -18.17^\circ$).

To define the total-magnetization of the interpretation model, we used the reduction to the pole technique (RTP) with the main field direction in the area. The RTP result (not shown) indicates that the magnetic source has purely induced magnetization. Alva-Valdivia et al. (2009) measured the magnetic susceptibility χ of carbonatitic samples of Jacupiranga alkaline complex, another southern Brazil complex in São Paulo state. They have found that the magnetic susceptibility for those samples varies from $\chi = 1.06 \times 10^{-3}$ SI to $\chi = 161.05 \times 10^{-3}$ SI (Alva-Valdivia et al. 2009, tb. 1). There are carbonatites with similar ages in both Jacupiranga and Anitápolis complexes (Gibson et al. 1999). So, we based the values for m_0 using this reference and the main magnetic field intensity of the Earth in the area ≈ 22768 nT. The magnetic susceptibility (χ) range used in this application is the upper axis in Fig. (11) which is equivalent to the m_0 axis.

The interpretation model is formed by an ensemble of $L = 8$ prisms, each one with number of polygon vertices $V = 30$ ($k = 1, \dots, 10$) describing the horizontal cross-sections of the polygons. We set the origin of the initial approximation $(x_0^k, y_0^k) = (6921, 688)$ km and the radii $r_j^k = 1500$ m so it involves the center and great part of the positive and negative poles of the anomaly. The depth extent of the prisms is $dz = 700$ m that returns a total-field anomaly in the same range of the observed data. Following the approach for the synthetic applications (sec. 3), we have inverted the real total-field anomaly (Fig. 10a) obtaining 100 different models. Each model was obtained by using a different pair of depth to the top z_0 and total-magnetization intensity m_0 (Fig. 11). The range of m_0 and z_0 in Fig. 11 were defined empirically, however, the m_0 range was based on the typical values of magnetic susceptibility for alkaline-carbonatitic rocks and the main field intensity for the study area. For all

the 100 models, the initial approximate has the same cylindrical shape and the regularization weights $\tilde{\alpha}_1 = 10^{-3}$, $\tilde{\alpha}_2 = 10^{-4}$, $\tilde{\alpha}_3 = 10^{-3}$, $\tilde{\alpha}_4 = 0$, $\tilde{\alpha}_5 = 0$, $\tilde{\alpha}_6 = 10^{-6}$, and $\tilde{\alpha}_7 = 10^{-5}$. Figs 5 and 8 show that lowest values for $\Gamma(\mathbf{p})$ (eq. 3) indicate the pair of m_0 and z_0 is close to the true one.

Therefore, we can interpret that the estimated model that has the pair $z_0 = -1200$ m and $m_0 = 2.5$ A/m (cyan diamond in Fig. 11) is more compatible with the possible values of magnetic susceptibility χ (upper axis in Fig. 11). We do not have evidences of an outcropping source for this anomaly, but there are evidences of outcropping intrusions in the area of the Anitápolis complex (Gibson et al. 1999). The depth to the top $z_0 = -1200$ indicates a very shallow source or a possible outcropping source. This estimated model produces a very low value for $\Gamma(\mathbf{p})$ (3) whose data fit is shown in Fig. 12a. The acceptable data fit is confirmed by the histogram of residuals in the inset of the 12a with μ close to zero and a low standard deviation similar to the synthetic applications. Fig. 12b shows the cylinder used as the initial approximate for the inversion. Figs 12c and d show the estimated model (red prisms) for this application. Our method estimated a body northwest-southeast elongated with volume 52.89 km^3 and total depth extent 5434.35 m ($dz = 679.29$). In addition, the magenta diamond in Fig. 11 is the estimated model that produces the lowest value for $\Gamma(\mathbf{p})$ (3). Nevertheless, both data fit and the estimated model (Figs 13a, c, and d) are very close to the cyan diamond solution (Fig. 12) in Fig. (11). The volume and total depth extent for this solution (Figs 13c and d) are, respectively, 48.37 km^3 and 5709.20 m ($dz = 713.65$). Both estimated models are very similar to each other, but the first one thicker and shallower than the second one. This difference is given by the inversion in order to compensate the estimated magnetic momentum for different values of z_0 and m_0 . So, considering the data fit and its histogram both solutions can be a possible geometry of this magnetic source in the Anitápolis complex. To confirm this estimated model, more prior geological information about this geological anomalous source must be included.

5 CONCLUSIONS

We have developed a 3-D radial inversion of total-field anomaly data to estimate the shape of an isolated 3-D geological body assuming the knowledge about its total-magnetization direction. We approximate the 3-D body by a set of vertically stacked right polygonal prisms with fixed depth to the top, thickness and total-magnetization vector. The horizontal cross-section of each prism is a polygon described by a given number of equally spaced radii from 0° to 360° connecting an arbitrary origin to the vertices of the polygon. We estimate the depth to the top and the total-magnetization intensity of the source using a validation test based on the minimization of the goal function. In this test, we run an inversion for a combination of ranges of depths to the top and total-magnetization intensities. The lowest value of the goal function indicates the optimal depth to the top and total-magnetic intensity. Our method defines the geometry of the 3-D geological source by estimating via an iterative nonlinear inversion algorithm the Cartesian coordinates of the arbitrary origin, the radii and the thickness of the prisms. For all the inversions, we set a cylinder shape as the initial approximate that involves part of the horizontal shape of the anomaly. To stabilize the inverse problem we introduced a set of seven constraints on the source shape.

This method is an extension of previous work that applied the set of polygonal prisms to estimate the shape of 3-D geological source by inverting gravity and gravity-gradient data. However, both of them assume the knowledge of the depth to the top and the physical property of the source. Also, they proposed a method to estimate by successive inversions the depth to the bottom of the source. In this work, we proposed a validation test to estimate both depth to the top and the physical property. Moreover, our method estimates the depth to bottom of the interpretation model introducing the thickness of the prisms as a parameter in the inverse problem. Unfortunately, our method does not guarantee the uniqueness of the solution due to the ambiguity of potential fields problems.

We have applied our method to an synthetic test simulating a symmetric source retrieving accurately the true model geometry. This example illustrates the efficiency of the constraints on the source's shape in an ideal case. Moreover, we have simulated a complex body to evaluate the performance of our method in a more realistic case. In this example, our method was capable to estimate a complex geometry with dipping and a variable shape along the depth. Both test were successfully achieved obtaining an estimated model that retrieve the source's shape and fits the data.

We applied our method to the total-field anomaly data of the alkaline-carbonatitic complex of Anitapolis, Santa Catarian state, Brazil. The estimated model shows a very complex geometry for the magnetic source that fits the observed data. Based on the map and histogram of residual, we interpret that this estimated model can be a possible geometry for the geological body.

A possible extension of this work is the inversion of a very elongated magnetic source or multiple

bodies. In addition, an inversion method combining gradient-based and heuristic approaches could be applied to estimate the optimal regularization weights for the set of seven constraints, overcoming problems with local minima.

ACKNOWLEDGMENTS

REFERENCES

- Alva-Valdivia, L. M., Perrin, M., Rivas-Sánchez, M. L., Goguitchaichvili, A., López-Loera, H., Lopes, O. F., & Bonás, T. B., 2009. Rock magnetism and microscopy of the jacupiranga alkaline-carbonatitic complex, southern brazil, *Earth, Planets and Space*, **61**(1), 161–171.
- Aster, R. C., Borchers, B., & Thurber, C. H., 2019. *Parameter Estimation and Inverse Problems*, Elsevier, 3rd edn.
- Ballantyne, E. J., 1980. Magnetic curve fit for a thin dike; calculator program (TI 59), *Geophysics*, **45**(3), 447–455.
- Barbosa, V. C. F., Silva, J. B. C., & Medeiros, W. E., 1997. Gravity inversion of basement relief using approximate equality constraints on depths, *Geophysics*, **62**, 1745–1757.
- Barbosa, V. C. F., Silva, J. B. C., & Medeiros, W. E., 1999b. Stable inversion of gravity anomalies of sedimentary basins with nonsmooth basement reliefs and arbitrary density contrast variations, *Geophysics*, **64**(3), 754–764.
- Bhattacharyya, B. K., 1980. A generalized multibody model for inversion of magnetic anomalies, *Geophysics*, **45**(2), 255–270.
- Cribb, J., 1976. Application Of The Generalized Linear Inverse To The Inversion Of Static Potential Data, *Geophysics*, **41**(6), 1365–1369.
- Dampney, C. N. G., 1969. The equivalent source technique, *Geophysics*, **34**(1), 39–53.
- Emilia, D. A., 1973. Equivalent sources used as an analytic base for processing total magnetic field profiles, *Geophysics*, **38**(2), 339–348.
- Gibson, S. A., Thompson, R. N., Leonardos, O. H., Dickin, A. P., & Mitchell, J. G., 1999. The limited extent of plume-lithosphere interactions during continental flood-basalt genesis: geochemical evidence from cretaceous magmatism in southern brazil, *Contributions to Mineralogy and Petrology*, **137**(1), 147–169.
- Golub, G. H. & Loan, C. F. V., 2013. *Matrix Computations (Johns Hopkins Studies in the Mathematical Sciences)*, Johns Hopkins University Press, 4th edn.
- Gomes, C. d. B., Comin-Chiaromonti, P., Azzone, R. A. G., Ruberti, E., & Rojas, G. E. E., 2018. Cretaceous carbonatites of the southeastern Brazilian Platform: a review, *Brazilian Journal of Geology*, **48**, 317 – 345.
- Horn, R. A. & Johnson, C. R., 1991. *Topics in Matrix Analysis*, Cambridge University Press, 1st edn.
- Li, W., Lu, W., Qian, J., & Li, Y., 2017. A multiple level-set method for 3d inversion of magnetic data, *GEOPHYSICS*, **82**(5), J61–J81.
- Li, Y. & Oldenburg, D. W., 1996. 3-D inversion of magnetic data, *Geophysics*, **61**(2), 394–408.
- Marquardt, D. W., 1963. An algorithm for least-squares estimation of nonlinear parameters, *Journal of the society for Industrial and Applied Mathematics*, **11**(2), 431–441.
- Oliveira Jr., V. C. & Barbosa, V. C. F., 2013. 3-D radial gravity gradient inversion, *Geophysical Journal International*, **195**(2), 883–902.
- Oliveira Jr., V. C., Barbosa, V. C. F., & Silva, J. B. C., 2011. Source geometry estimation using the mass

- excess criterion to constrain 3-D radial inversion of gravity data, *Geophysical Journal International*, **187**(2), 754–772.
- Oliveira Jr., V. C., Sales, D., Barbosa, V. C. F., & Uieda, L., 2015. Estimation of the total magnetization direction of approximately spherical bodies, *Nonlinear Processes in Geophysics*, **22**(2).
- Pignatelli, A., Nicolosi, I., & Chiappini, M., 2006. An alternative 3d inversion method for magnetic anomalies with depth resolution, *Annals of geophysics = Annali di geofisica*.
- Pilkington, M., 1997. 3-D magnetic imaging using conjugate gradients, *Geophysics*, **62**(4), 1132–1142.
- Plouff, D., 1976. Gravity and magnetic fields of polygonal prisms and application to magnetic terrain corrections, *Geophysics*, **41**(4), 727–741.
- Silva, J. B. C. & Hohmann, G. W., 1983. Nonlinear magnetic inversion using a random search method, *Geophysics*, **48**(12), 1645–1658.
- Uieda, L., Oliveira Jr., V. C., & Barbosa, V. C. F., 2013. Modeling the earth with fatiando a terra, in *Proceedings of the 12th Python in Science Conference*, pp. 96 – 103.
- Wang, X. & Hansen, R. O., 1990. Inversion for magnetic anomalies of arbitrary three-dimensional bodies, *Geophysics*, **55**(10), 1321–1326.
- Zhang, H., Ravat, D., Marangoni, Y. R., Chen, G., & Hu, X., 2018. Improved total magnetization direction determination by correlation of the normalized source strength derivative and the reduced-to-pole fields, *Geophysics*, **83**(6), J75–J85.

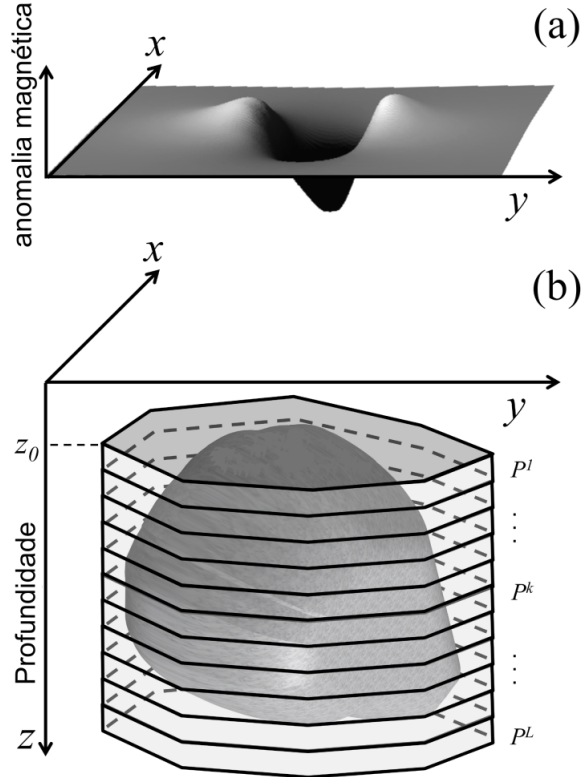


Figure 1. Schematic representation of (a) total-field anomaly (gray surface) produced by (b) a 3-D anomalous source (dark gray volume). The interpretation model in (b) consists of a set of L vertical, juxtaposed 3-D prisms P^k , $k = 1, \dots, L$, (light gray prisms) in the vertical direction of a right-handed coordinate system.

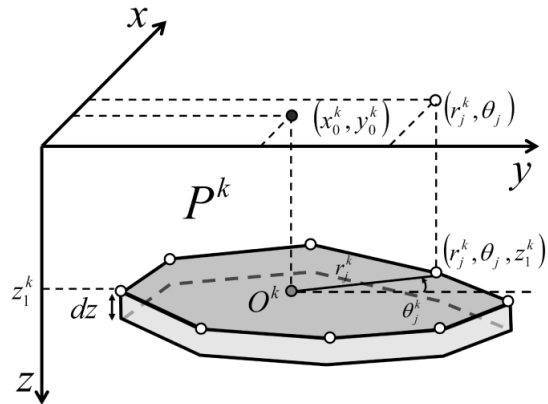


Figure 2. Polygonal cross-section of the k th vertical prism P^k described by V vertices (white dots) with polar coordinates (r_j^k, θ_j^k) , $j = 1, \dots, V$, $k = 1, \dots, L$, referred to an arbitrary origin O^k (grey dot) with horizontal Cartesian coordinates (x_0^k, y_0^k) , $k = 1, \dots, L$.

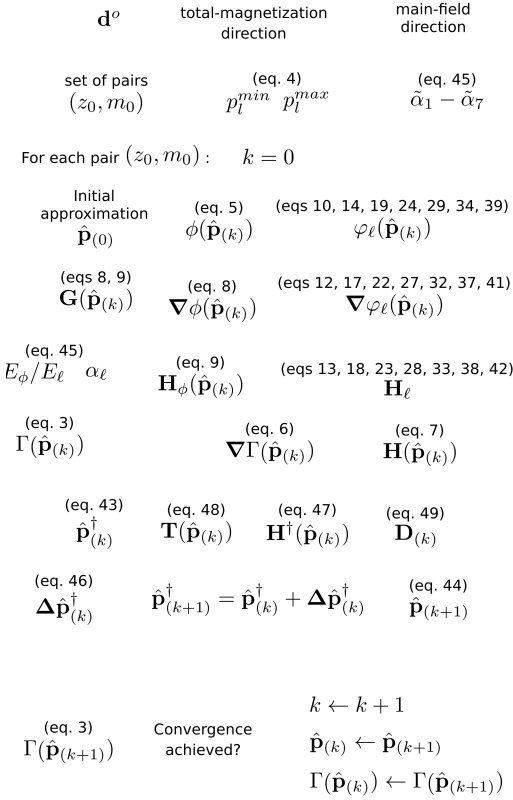


Figure 3. Flowchart of our algorithm.

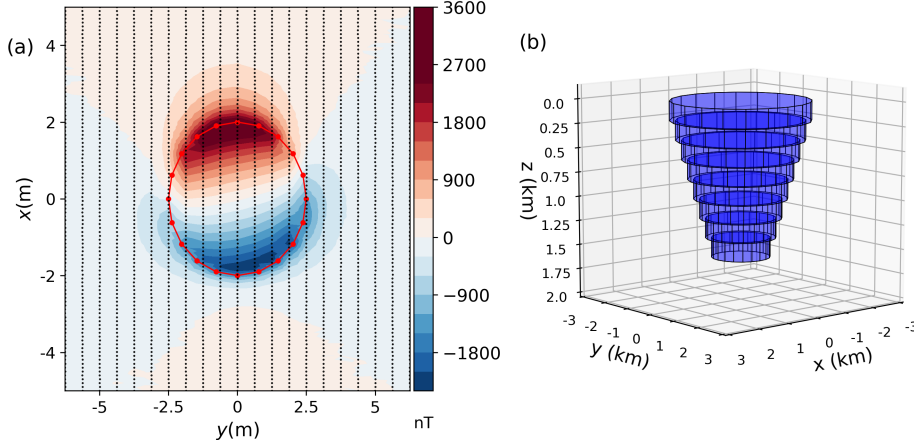


Figure 4. Simple model simulation. (a) noise-corrupted total-field anomaly produced by the simple model (blue prisms) in (b) with a pseudorandom Gaussian distribution having mean $\mu_0 = 0$ nT and standard deviation $\sigma_0 = 5$ nT, the black dots represent the observation points. The connected red dots are the vertices of the initial approximate horizontally projected at the data map. (b) perspective view of the simple model represented by the blue prisms.

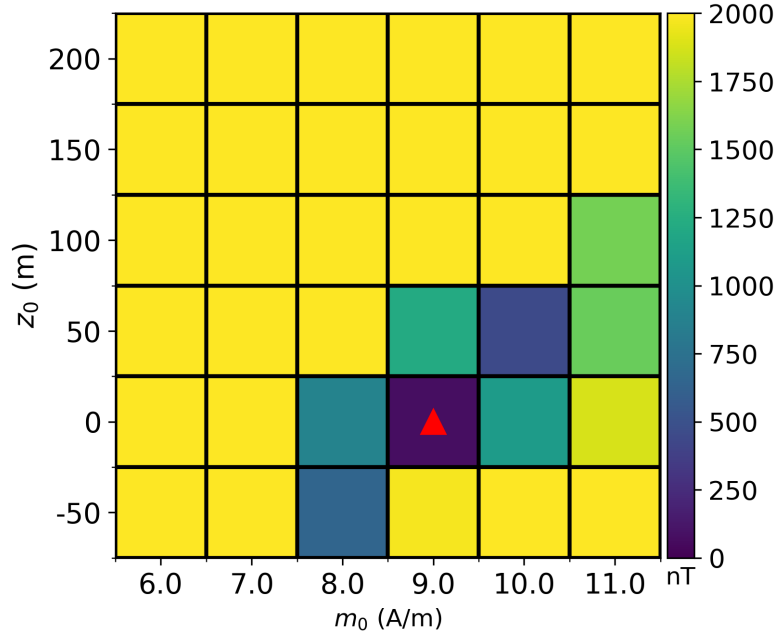


Figure 5. Validation to estimate the depth to the top (z_0) and the total-magnetization intensity (m_0) for the simple model application. The ranges in the axes are $m_0 = 6$ A/m to $m_0 = 11$ A/m with 1 A/m intervals and $z_0 = -50$ m to 200 m with 50 m intervals. Each square is the $\Gamma(\mathbf{p})$ (eq. 3) in nT produced by an estimated model inverted using a pair of m_0 and z_0 . These 36 inversions were computed using the same cylinder as a initial approximation. The red triangle represents the true m_0 and z_0 .

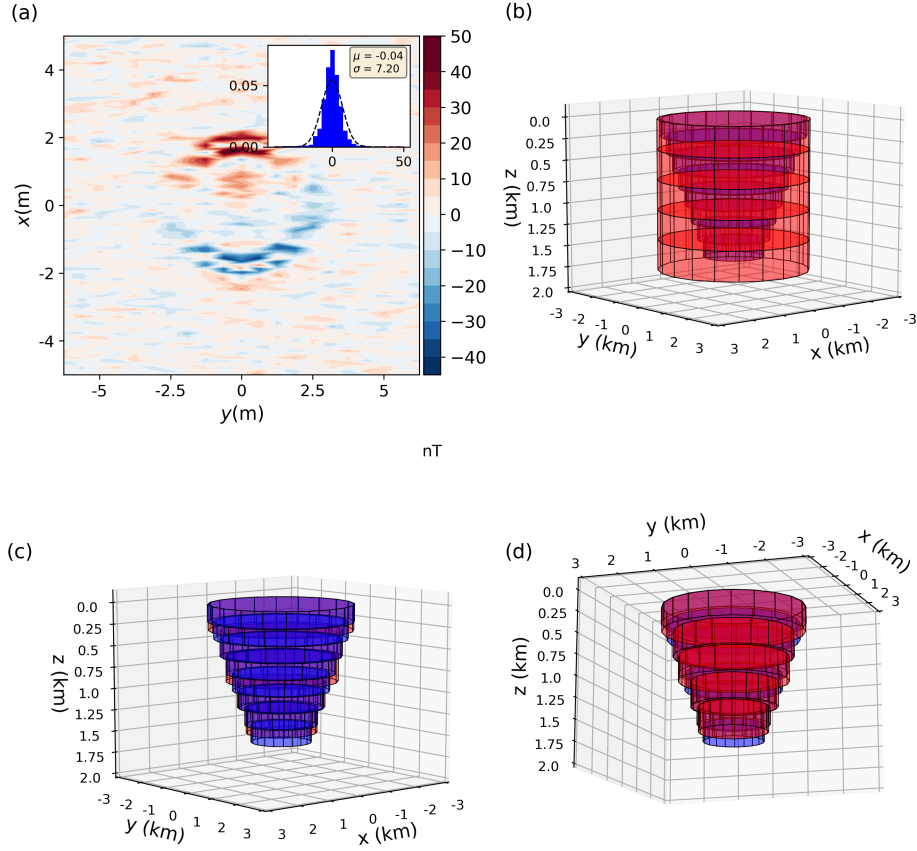


Figure 6. Application to simple model data. (a) residual data given by the difference between the noise-corrupted data (Fig. 4a) and the predicted data (not shown) produced by the estimated model. The inset in (a) shows the histogram of the residuals and the Gaussian curve (dashed line) (dashed line) whose mean and standard deviation are, respectively, $\mu = 0.04$ nT and $\sigma = 7.20$ nT. (b) perspective view of the initial approximate (red prisms) and the true model (blue prisms). (c) and (d) comparison between the estimated source (red prisms) and the true model (blue prisms) in perspective views.

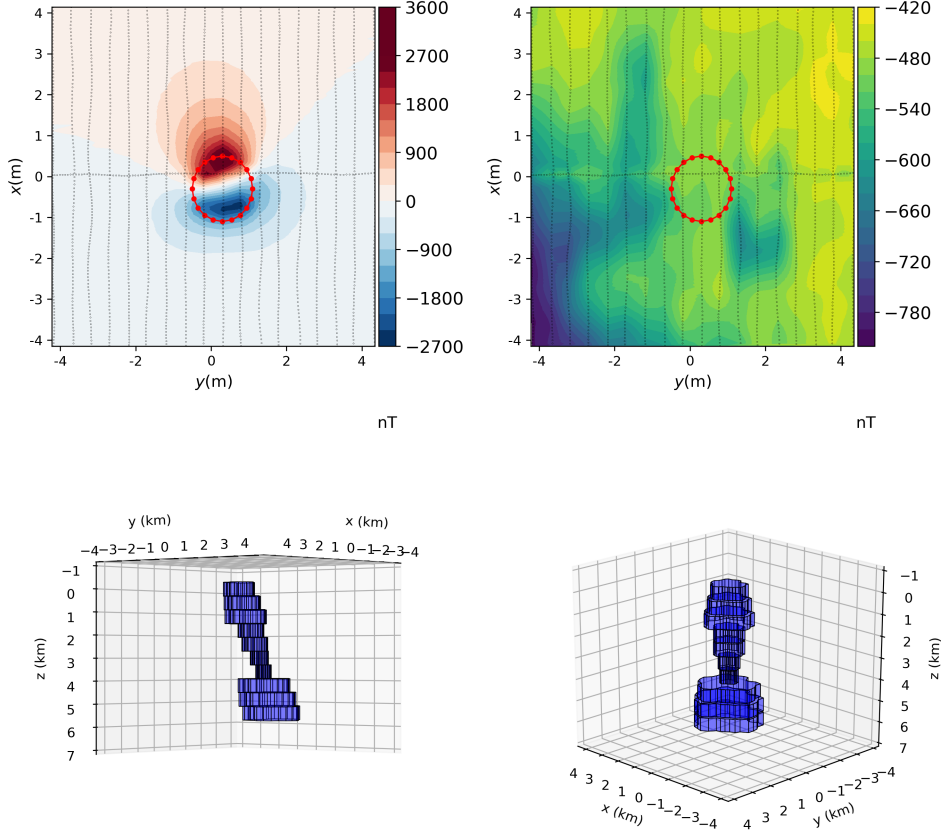


Figure 7. Complex model simulation. (a) noise-corrupted total-field anomaly with a pseudorandom Gaussian distribution having mean $\mu_0 = 0$ nT and standard deviation $\sigma_0 = 5$ nT produced by the complex model, the black dots represent the observation points. The connected red dots are the vertices of the initial approximate horizontally projected at the data map. (b) elevation of the observations simulating an airborne survey. (c) and (d) perspective views of the complex model represented by the blue prisms.

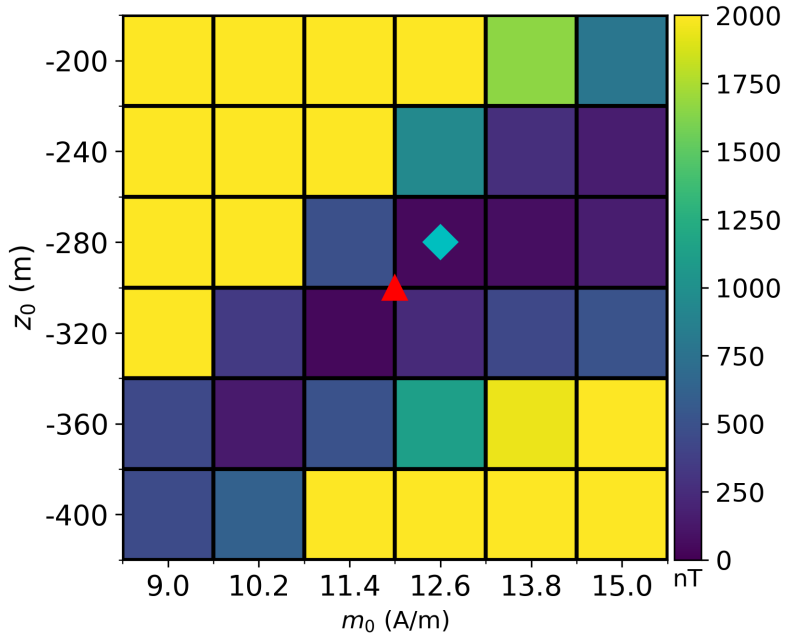


Figure 8. Validation to estimate the depth to the top (z_0) and the total-magnetization intensity (m_0) for the complex model application. The ranges in the axes are $m_0 = 9$ A/m to $m_0 = 15$ A/m with 1.2 A/m intervals and $z_0 = -400$ m to -200 m with 40 m intervals. Each square is the $\Gamma(\mathbf{p})$ (eq. 3) in nT produced by an estimated model inverted using a pair of m_0 and z_0 . These 36 inversions were computed using the same cylinder as a initial approximation. The red triangle represents the true m_0 and z_0 . The cyan diamond represents the estimated model that produces the lowest value for $\Gamma(\mathbf{p})$ (eq. 3).

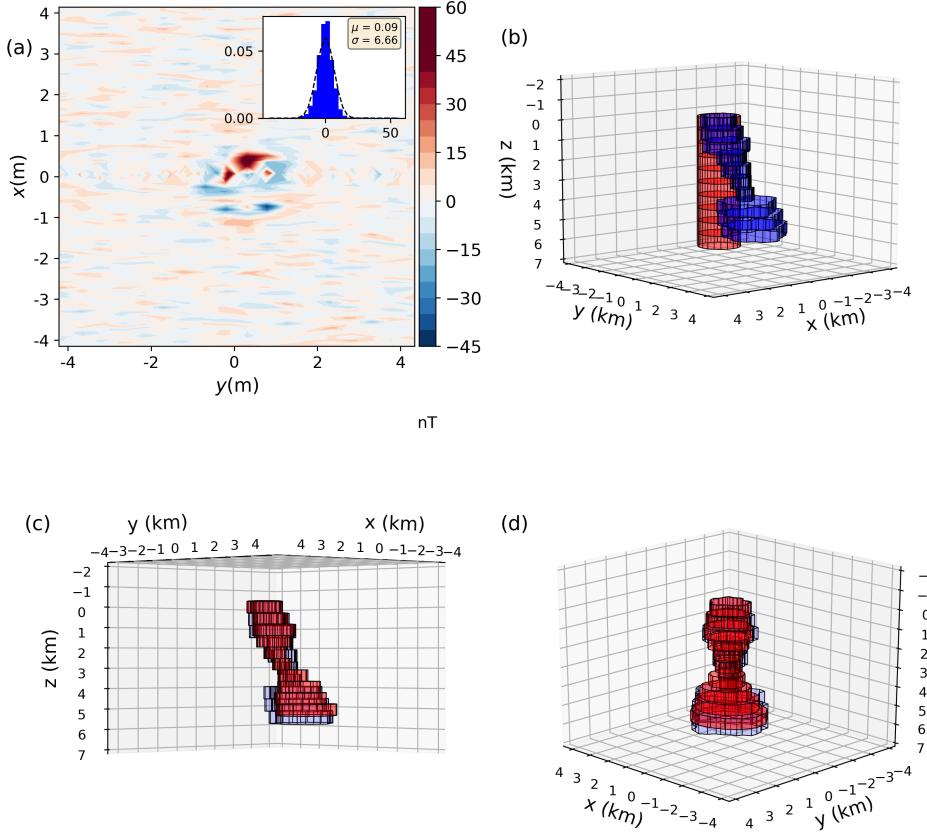


Figure 9. Application to complex model data. (a) residual data given by the difference between the noise-corrupted data (Fig. 7a) and the predicted data (not shown) produced by the estimated model. The inset in (a) shows the histogram of the residuals and the Gaussian curve (dashed line) whose mean and standard deviation are, respectively, $\mu = 0.09$ nT and $\sigma = 6.66$ nT. (b) perspective view of the initial approximate (red prisms) and the true model (blue prisms). (c) and (d) comparison between the estimated source (red prisms) and the true model (blue prisms) in perspective views.

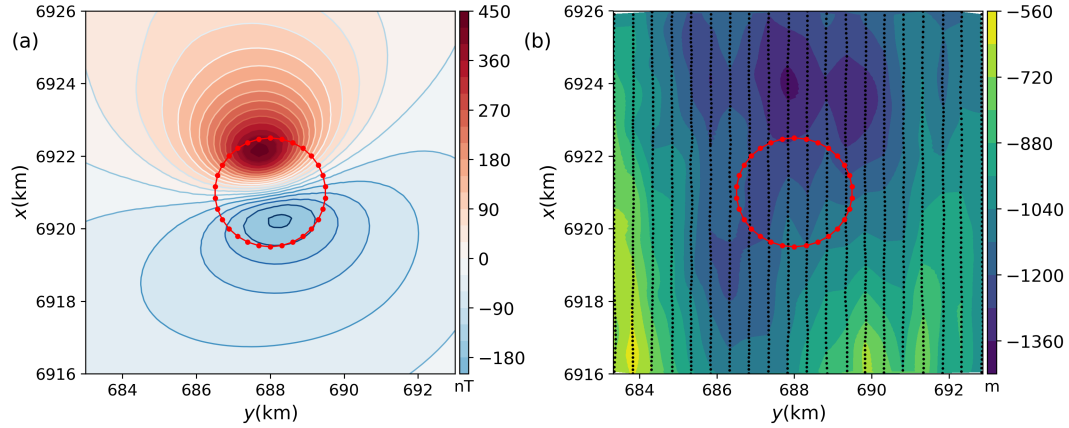


Figure 10. (a) Total-field anomaly of the alkaline-carbonatitic complex of Anitapolis processed and calculated at $z = -2000$ m using upward continuation. The magnetic data are in nT and the coordinates are in UTM on the WGS84 datum, with central meridian 51° W. (b) GPS elevation of the observation points in m. The black dots are the measures of the original data. The connected red dots in both maps are the vertices of the initial approximate horizontally projected at the data map.

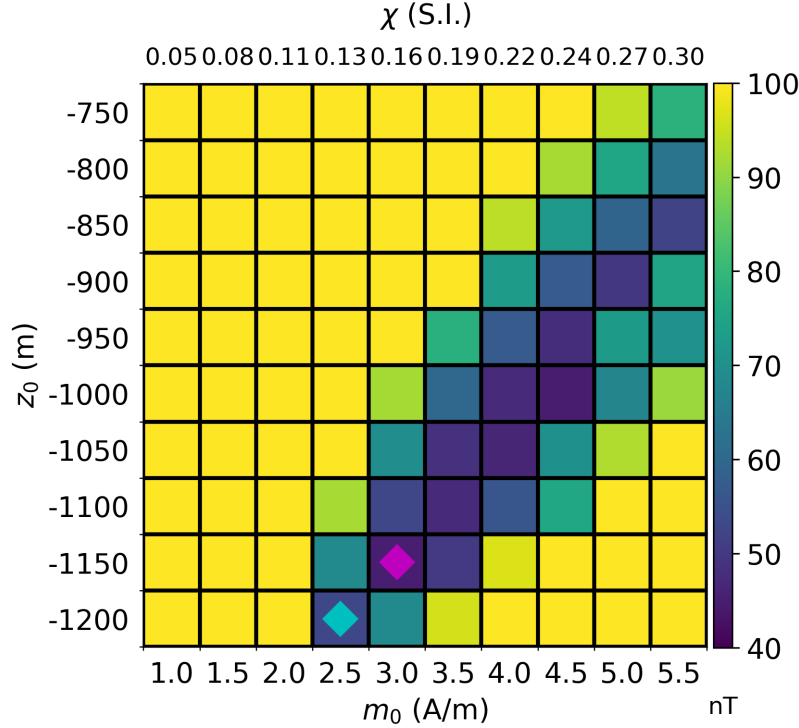


Figure 11. Validation to estimate the depth to the top (z_0) and the total-magnetization intensity (m_0) for the field application. The ranges in the axes are $m_0 = 1$ A/m to $m_0 = 5.5$ A/m with 0.5 A/m intervals and $z_0 = -1200$ m to -750 m with 30 m intervals. This range of m_0 corresponds to an interval of magnetic susceptibility χ from 0.05 to 0.30 (upper axis). Each square is the goal function $\Gamma(\mathbf{p})$ (eq. 3) produced by an estimated model inverted using a pair of m_0 and z_0 . These 100 inversions were computed using the same cylinder as a initial approximation. The cyan diamond represents the estimated model whose magnetic susceptibility is compatible to the main field intensity. The magenta diamond represents the estimate model that produces the lowest value of $\Gamma(\mathbf{p})$ (eq. 3).

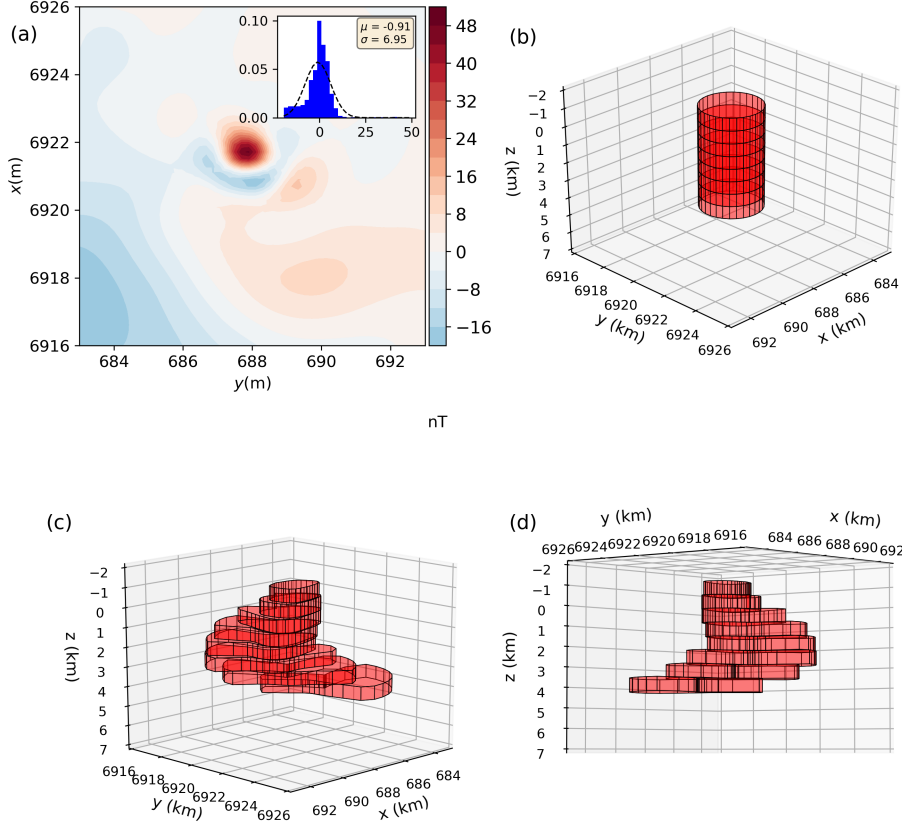


Figure 12. Application to field data represented by the cyan diamond in Fig. 11. (a) residual data given by the difference between the observed data (Fig. 10a) and the predicted data (not shown). The inset in (a) shows the histogram of the residuals and the Gaussian curve (dashed line) whose mean and standard deviation are, respectively, $\mu = 0.91$ nT and $\sigma = 6.95$ nT. (b) perspective view of the initial approximate (red prisms). (c) and (d) perspective views of the estimated model (red prisms).

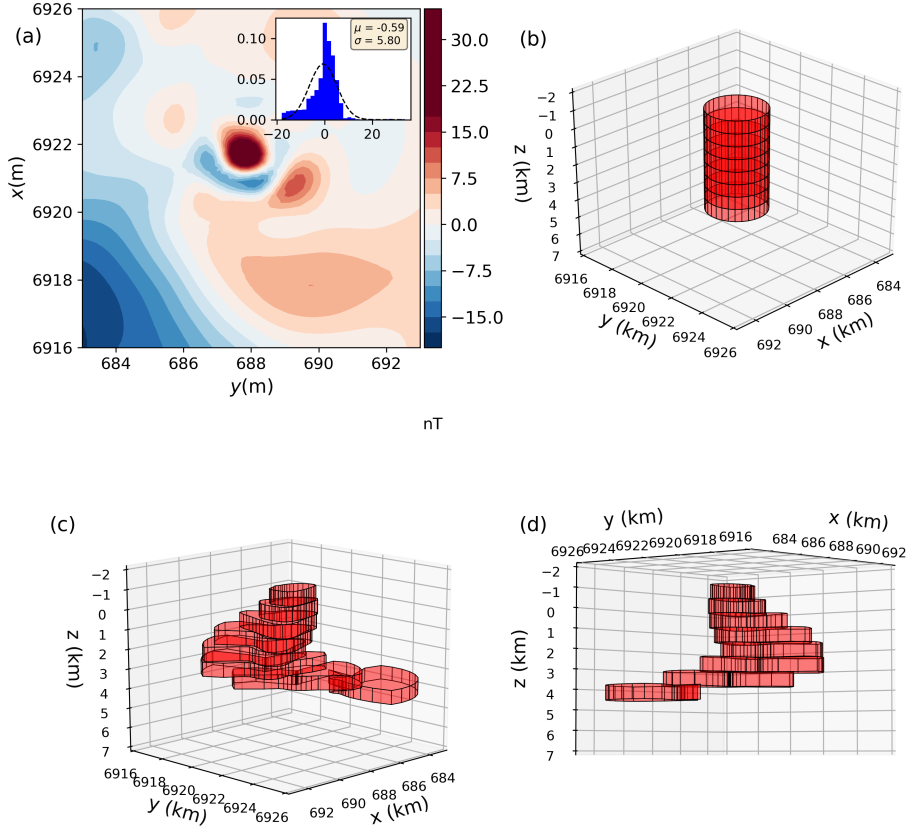


Figure 13. Application to field data represented by the magenta diamond in Fig. 11. (a) residual data given by the difference between the observed data (Fig. 10a) and the predicted data (not shown). The inset in (a) shows the histogram of the residuals and the Gaussian curve (dashed line) whose mean and standard deviation are, respectively, $\mu = -0.59$ nT and $\sigma = 5.80$ nT. (b) perspective view of the initial approximate (red prisms). (c) and (d) perspective views of the estimated model (red prisms).